

See discussions, stats, and author profiles for this publication at: <https://www.researchgate.net/publication/225183805>

Silver Nanoparticle Monolayer-to-Bilayer Transition at the Air/Water Interface as Studied by the GISAXS Technique: Application of a New Paracrystal Model

ARTICLE *in* LANGMUIR · JUNE 2012

Impact Factor: 4.46 · DOI: 10.1021/la301577a · Source: PubMed

CITATIONS

9

READS

25

9 AUTHORS, INCLUDING:



Karol Vegso

Slovak Academy of Sciences

43 PUBLICATIONS 102 CITATIONS

SEE PROFILE



Matej Jergel

Slovak Academy of Sciences

285 PUBLICATIONS 1,219 CITATIONS

SEE PROFILE



Martin Weis

Slovak University of Technology in Bratislava

143 PUBLICATIONS 840 CITATIONS

SEE PROFILE



Eva Majkova

Slovak Academy of Sciences

206 PUBLICATIONS 860 CITATIONS

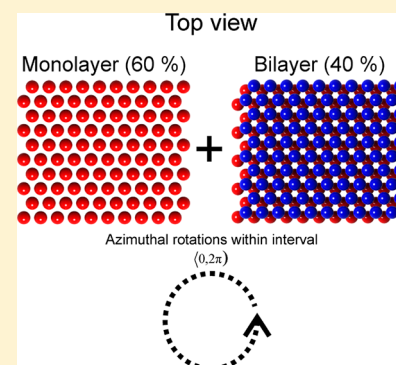
SEE PROFILE

Silver Nanoparticle Monolayer-to-Bilayer Transition at the Air/Water Interface as Studied by the GISAXS Technique: Application of a New Paracrystal Model

K. Vegso,^{*,†} P. Siffalovic,[†] M. Jergel,[†] M. Weis,[†] M. Benkovicova,[†] E. Majkova,[†] S. Luby,[†] T. Kocsis,[†] and I. Capek[‡]

[†]Institute of Physics and [‡]Polymer Institute, Slovak Academy of Sciences, Dubravská cesta 9, 84511 Bratislava, Slovakia

ABSTRACT: An original diffraction model for the analysis of grazing-incidence small-angle X-ray scattering (GISAXS) from the nanoparticle Langmuir films was developed. This model relies on the concept of the 2D hexagonal paracrystal and employs the distorted-wave Born approximation that is relevant for GISAXS measurements at the air/water interface when the angle of incidence is close to the critical value. The model comprises the cases of the close-packed nanoparticle monolayer and bilayer with the AB-type layer stacking. In this way, both the lateral (along the interface) and vertical (normal to the interface) correlations of the nanoparticle positions can be analyzed. The model was applied to an in situ GISAXS study of the formation of a silver nanoparticle Langmuir film during compression at the air/water interface in the Langmuir–Blodgett trough. Spherical nanoparticles of 5.8 ± 0.6 nm diameter were employed. Different compression stages starting from the submonolayer up to the monolayer collapse via bilayer formation were analyzed in terms of the mean lateral interparticle distance, degree of paracrystal disorder, interlayer distance, vertical disorder, and layer-stacking type in the bilayer as well as the ratio between the monolayer and bilayer coverage in the final film. The model developed is applicable to any nanoparticle Langmuir film formed at the air/liquid interface to extract structural parameters on the nanoscale. The particular results obtained have direct implications on the preparation of silver plasmonic templates with “hot spots” for surface-enhanced Raman scattering.



INTRODUCTION

Ordered assemblies of chemically synthesized nanoparticles are the subject of permanent interest that is driven by the development of novel nanoscale materials. Several techniques were utilized to prepare highly ordered 2D and 3D nanostructures from colloidal metallic nanoparticle solutions such as Langmuir–Blodgett (LB) and Langmuir–Schaefer (LS) depositions and drop casting followed by solvent evaporation or spin coating.^{1–3} The LB and LS techniques are especially suitable for the fabrication of uniform close-packed nanoparticle monolayers over large areas. Here, an ordered nanoparticle array floating at the air/water interface (Langmuir film) is formed at an appropriate surface pressure that is controlled by movable barriers in the Langmuir–Blodgett trough.⁴ The metallic nanoparticles covered with a hydrophobic surfactant shell can self-assemble into close-packed islands with hexagonal symmetry (submonolayer) after the application of their colloidal solution to the water surface.^{5,6} The islands merge into a compact nanoparticle monolayer with increasing surface pressure before the collapse to a bilayer structure starts.^{6,7} Here, it should be noted that not all nanoparticle Langmuir films transform from monolayers to bilayers under compression. For example, thiol-ligated Au nanoparticles form trilayer structures at the air–water interface.^{8,9} There are several stages of nanoparticle Langmuir film formation visible in the surface pressure–area isotherm. The underlying structural changes in the nanoparticle order were studied by direct imaging techniques such as Brewster angle or phase contrast microscopy

that provide information on the microscale.¹⁰ The electron microscopy used to visualize the nanoparticle order is inapplicable because of the high vapor pressure and surface tension of the water subphase. Hence, the X-ray scattering techniques are the main investigation tool for the nanoscale.

Specular X-ray reflectivity (XRR) and grazing-incidence small-angle X-ray scattering (GISAXS) were used to detect the nanoparticle order at the air/water interface in the Langmuir–Blodgett trough.^{11–13} Because they provide information about the reciprocal space, structural models have to be adopted to evaluate the results. Here, the approaches known from traditional crystallography may be applied where atoms or molecules are replaced by nanoparticles. Moreover, the nanoparticle size dispersion must be considered. A close-packed hexagonal structure with paracrystal disorder was usually detected in the nanoparticle monolayers fabricated by the LS or LB technique.¹⁴ The paracrystal exhibits a correlation between neighboring lattice sites that gradually vanishes for the more distant ones because of the disorder accumulation.^{15,16} Therefore, the paracrystal model is a statistical model suitable for the interpretation of diffraction data from the short-range-ordered structures. A broadening of the diffraction peaks with increasing diffraction angle differentiates this type of disorder

Received: April 19, 2012

Revised: May 31, 2012

Published: June 4, 2012

from the random noncumulative one in the long-range-ordered structures.

In this article, we present an original diffraction model for the evaluation of the GISAXS patterns from the close-packed nanoparticle monolayer and bilayer that is based on the concept of an ideal 2D hexagonal paracrystal as proposed by Eads and Millane.¹⁷ The model employs the distorted-wave Born approximation (DWBA)¹⁸ to incorporate the multiple scattering effects typical for GISAXS and allows us to distinguish between different types of the lateral (along the interface) and vertical (normal to the interface) correlations of the nanoparticle positions. Theoretical aspects of the model are discussed to define its applicability. The model is applied to an in situ study of the formation of a silver nanoparticle Langmuir film during compression at the air/water interface in the Langmuir–Blodgett trough. Different compression stages up to the monolayer collapse via bilayer formation are analyzed in terms of the mean lateral interparticle distance, degree of paracrystal disorder, interlayer distance and vertical disorder in the newly formed bilayer, layer stacking type, and ratio between the monolayer and bilayer coverage in the final film. To our knowledge, such a rigorous analysis to reveal details of the nanoparticle monolayer collapse at the air/water interface down to the level of nanoparticle order has never yet been done. The model developed is applicable to any nanoparticle Langmuir film formed at the air/liquid interface to extract structural parameters on the nanoscale. The particular results obtained have direct implications for the optimization of the LB and LS depositions to prepare silver plasmonic templates with “hot spots” for surface-enhanced Raman scattering and other plasmonic applications.

EXPERIMENTAL DETAILS

Details of the chemical synthesis of the silver nanoparticles were published elsewhere.¹³ The diameter of the spherical nanoparticles determined from small-angle X-ray scattering (SAXS) was 5.8 ± 0.6 nm. The colloidal nanoparticle solution was dried at room temperature to evaporate toluene. The dried nanoparticles were redissolved in chloroform (Sigma-Aldrich) and spread on the water subphase ($18.2 \text{ m}\Omega\text{-cm}$, Elga, Bucks) by a microsyringe (Hamilton, Reno, NV). The total working area of the Langmuir–Blodgett trough used (KSV, Nima Technology) was 550 cm^2 . The monolayer was allowed to equilibrate for 30 min before the compression. This time was found to be sufficient for solvent evaporation and submonolayer formation. The submonolayer was continuously compressed at a rate of $7 \text{ cm}^2/\text{min}$ from an initial surface pressure of 9.8 mN/m up to a final pressure of 37.7 mN/m . The surface pressure–area isotherm was measured by the Wilhelmy plate method using a PS4 surface-pressure sensor (Nima Technology).

The SAXS and GISAXS measurements were performed in an original laboratory setup that allows real-time studies of nanoparticle kinetics at the air/water interface. A microfocus X-ray source with Montel optics ($1\mu\text{S}$, Incoatec) delivers a focused X-ray beam (0.154 nm wavelength) with a spot size of $250 \mu\text{m}$ (fwhm) at a focal length of 56 cm (5 mrad divergence) and a total flux of 3.3×10^8 photons/s. A fast 2D X-ray detector (Pilatus 100K, Dectris) was employed. The pixel size of the Pilatus detector is $172 \times 172 \mu\text{m}^2$. Further details of the experimental X-ray setup may be found elsewhere.^{13,19} The GISAXS measurements were performed at an angle of incidence of 0.1° , which is below the critical angle of water, 0.15° . The distance between the center of the Langmuir–Blodgett trough and the detector was set to 0.53 m . The corresponding angular resolution is then given by the ratio between the pixel size and the sample–detector distance and is equal to $3.2 \times 10^{-1} \text{ mrad}$. In addition, the 2D GISAXS patterns were calibrated with a silver behenate standard (Sigma-Aldrich). The GISAXS evolution during the barrier compression was measured as a series of 2D frames (movie), each with a 0.5 s exposition time.

Moreover, two 1200 frame series were measured under static conditions before and after the compression.

Diffraction Model of GISAXS from the Nanoparticle Monolayer and Bilayer. Let us consider a 1D lattice in the (x, y) plane with paracrystal disorder that has uncorrelated x and y components. Disorder may occur in an arbitrary direction around the lattice point. The position vector d_n of the n th lattice point (the n th nanoparticle in our case) with respect to the neighboring $(n-1)$ th one is expressed by the recurrence formula

$$d_n = d_{n-1} + (\langle d \rangle + g_{x,n}, g_{y,n}) \text{ or } d_n = \left(n\langle d \rangle + \sum_{k=0}^n g_{x,k}, \sum_{k=0}^n g_{y,k} \right) \quad (1)$$

where $\langle d \rangle$ represents the mean nearest-neighbor (interparticle) distance and g_x and g_y are Gaussian random variables oriented along the x and y axes with zero mean values, respectively (Figure 1). The positions of the

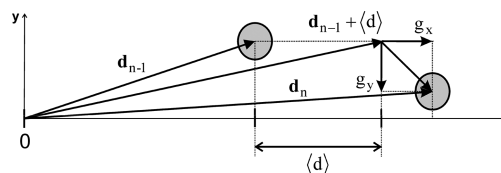


Figure 1. Construction of the position vector of the n th nanoparticle d_n starting from the $(n-1)$ th one d_{n-1} in the 1D paracrystal. The quantity $\langle d \rangle$ is the interparticle distance between the neighboring nanoparticles and g_x and g_y are the zero-mean random variables with normal distribution oriented along the x and y axes, respectively.

neighboring nanoparticles are correlated, and sums $\sum_{k=0}^n g_{x,k}$ and $\sum_{k=0}^n g_{y,k}$ represent the disorder that is gradually accumulated up to the n th nanoparticle in the row. Let us further assume that g_x and g_y random variables have an identical variance of $\sigma_x^2 = \sigma_y^2 = \sigma^2$. The 1D paracrystal is thus fully described by the mean vector $d = \langle d_n \rangle$ and Gaussian random variables g_x and g_y and their variance σ^2 .

In the following text, we assume two mutually rotated 1D paracrystals as described above with mean vectors $a = \langle a_n \rangle$ and $b = \langle b_n \rangle$ in the (x, y) plane that together make an angle of 60° (Figure 2).

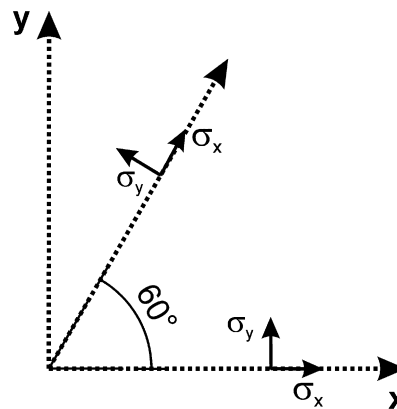


Figure 2. Construction of the ideal hexagonal nanoparticle paracrystal from two independent 1D ones. The first 1D paracrystal stretches along the x axis, and the second one is inclined by 60° with respect to the x axis. The σ_x and σ_y quantities are standard deviations of the 1D paracrystal defined along the x and y axes, respectively.

Their mean interparticle distances $\langle d \rangle$ and variances σ^2 are identical. From the a_n and b_n vectors, an ideal hexagonal 2D paracrystal of $N \times N$ nanoparticles located at $d_{mn} = a_m + b_n$ positions can be built with the lateral degree of disorder defined by the $\sigma/\langle d \rangle$ ratio. In other words, the 2D paracrystal is obtained from a convolution of two 1D

paracrystals.¹⁵ If the mean position vector $\langle a_m \rangle$ averaged over the vectors

$$a_m = \langle m \rangle d + \sum_{k=0}^m g_{x,k} \sum_{k=0}^m g_{y,k} \quad (2)$$

is oriented along the x axis, then position vectors b_n rotated by 60° in the same orthogonal coordinate system read

$$b_n = \left(\frac{1}{2} \left[n \langle d \rangle + \sum_{l=0}^n g_{x,l} \right] - \frac{\sqrt{3}}{2} \sum_{l=0}^n g_{y,l}, \frac{\sqrt{3}}{2} \left[n \langle d \rangle + \sum_{l=0}^n g_{x,l} \right] + \frac{1}{2} \sum_{l=0}^n g_{y,l} \right) \quad (3)$$

Consequently, the structure factor of the ideal hexagonal 2D paracrystal is given by the multiplication of the respective 1D structure factors

$$S(q_x, q_y) = S_1(q_x, q_y) S_2(q_x, q_y) \quad (4)$$

where $S_1(q_x, q_y)$ and $S_2(q_x, q_y)$ are defined as

$$S_1(q_x, q_y) = N + \sum_{m=0}^{N-1} \sum_{m' \neq m}^{N-1} \exp(iq_x(m-m')\langle d \rangle) \times \exp\left(iq_x \left(\sum_{k=0}^m g_{x,k} - \sum_{k'=0}^{m'} g_{x,k'} \right)\right) \times \exp\left(iq_y \left(\sum_{k=0}^m g_{y,k} - \sum_{k'=0}^{m'} g_{y,k'} \right)\right) \quad (5)$$

$$S_2(q_x, q_y) = N + \sum_{n=0}^{N-1} \sum_{n' \neq n}^{N-1} \exp\left(i \left(\frac{1}{2} q_x + \frac{\sqrt{3}}{2} q_y \right) (n-n') \langle d \rangle \right) \times \exp\left(i \left(\frac{1}{2} q_x + \frac{\sqrt{3}}{2} q_y \right) \left(\sum_{l=0}^n g_{x,l} - \sum_{l'=0}^{n'} g_{x,l'} \right)\right) \times \exp\left(i \left(-\frac{\sqrt{3}}{2} q_x + \frac{1}{2} q_y \right) \left(\sum_{l=0}^n g_{y,l} - \sum_{l'=0}^{n'} g_{y,l'} \right)\right) \quad (6)$$

Here, q_x and q_y are the lateral coordinates in the reciprocal space oriented along the interface. Before averaging over random variables g_x and g_y , eqs 5 and 6 must be modified to a more usable form. To do so, eq 5 can be rewritten as

$$\langle S_1(q_x, q_y) \rangle = N + \sum_{m=0}^{N-1} \sum_{m'=0}^{m-1} \exp(iq_x(m-m')\langle d \rangle) \times \left\langle \exp\left(iq_x \sum_{k=m'+1}^m g_{x,k}\right) \right\rangle \left\langle \exp\left(iq_y \sum_{k=m'+1}^m g_{y,k}\right) \right\rangle + \sum_{m=0}^{N-1} \sum_{m'=m+1}^{N-1} \exp(iq_x(m-m')\langle d \rangle) \times \left\langle \exp\left(-iq_x \sum_{k=m+1}^{N-1} g_{x,k}\right) \right\rangle \left\langle \exp\left(-iq_y \sum_{k=m+1}^{N-1} g_{y,k}\right) \right\rangle \quad (7)$$

where the symbol $\langle \dots \rangle$ means a statistical averaging over g_x and g_y . Similarly, as in the case of the 1D paracrystal model, we can apply a

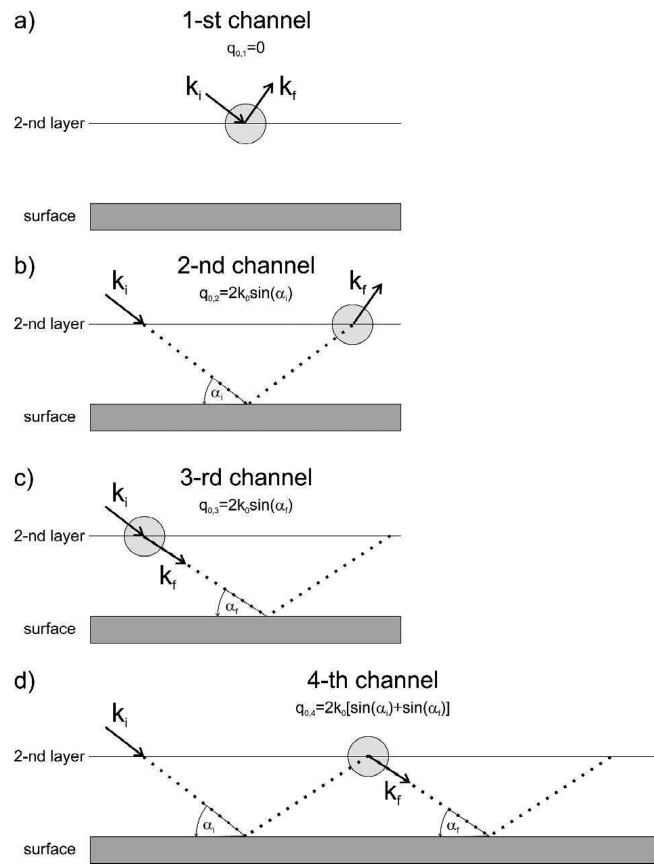


Figure 3. Four scattering events considered in DWBA for a nanoparticle in the second layer. (a) Kinematic scattering of the incident wave on the nanoparticle, (b) reflection of the incident wave on the surface followed by scattering on the nanoparticle, (c) scattering of the incident wave on the nanoparticle followed by reflection on the surface (d) reflection of the incident wave on the surface followed by scattering on the nanoparticle and another reflection on the surface. Additional optical paths of the waves traveling between the second layer and the substrate are drawn by the dotted lines.

substitution^{15,16}

$$\left\langle \exp\left(\pm iq \sum_{k=1}^m g_k\right) \right\rangle = \exp\left(-\frac{1}{2}mq^2\sigma^2\right) \quad (8)$$

where q is a reciprocal space coordinate, g_k is a random variable with a normal distribution, and $\langle g_k^2 \rangle = \sigma^2$ is its variance. By applying eq 8 and some algebra,^{15,16} we find that the averaged eq 7 takes a more applicable form

$$\langle S_1(q_x, q_y) \rangle = N + 2 \sum_{k=1}^{N-1} (N-k) \cos(kq_x \langle d \rangle) \times \exp\left(-\frac{1}{2}k\sigma^2(q_x^2 + q_y^2)\right) \quad (9)$$

Similarly, the averaging in eq 6 results in the equation^{15,16}

$$\langle S_2(q_x, q_y) \rangle = N + 2 \sum_{l=1}^{N-1} (N-l) \cos\left(l \left(\frac{1}{2} q_x + \frac{\sqrt{3}}{2} q_y \right) \langle d \rangle \right) \times \exp\left(-\frac{1}{2}l\sigma^2(q_x^2 + q_y^2)\right) \quad (10)$$

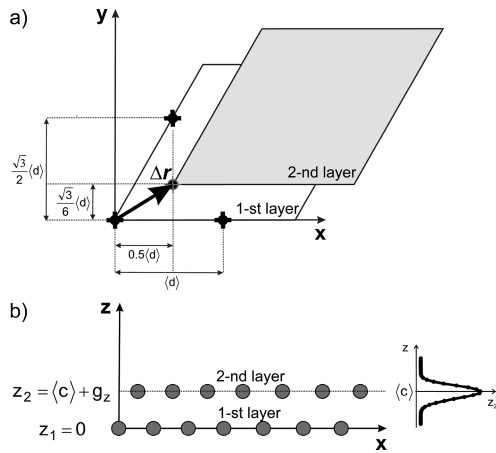


Figure 4. (a) Construction of the nanoparticle bilayer with hexagonal paracrystal disorder in the layers. The quantity Δr is the translation vector between the first and second layers in the AB-stacked structure. (b) Vertical position of the second layer z_2 with a normal distribution around the mean interlayer distance $\langle c \rangle$.

The total X-ray intensity (or cross section) scattered by the hexagonal nanoparticle monolayer with paracrystal disorder is given by the equation¹⁴

$$I(q_x, q_y, k_{z,i}, k_{z,f}) = \langle |F(q_x, q_y, k_{z,i}, k_{z,f}, R)|^2 \rangle_R \langle S_1(q_x, q_y) \rangle \times \langle S_2(q_x, q_y) \rangle \quad (11)$$

where the symbol $\langle \dots \rangle_R$ means averaging over the size distribution of the nanoparticles and the function

$$F(q_x, q_y, k_{z,i}, k_{z,f}, R) = F_1(q_x, q_y, q_{z,1}, R) + F_2(q_x, q_y, q_{z,2}, R) + F_3(q_x, q_y, q_{z,3}, R) + F_4(q_x, q_y, q_{z,4}, R) \quad (12)$$

is the form factor of a spherical nanoparticle with radius R in DWBA. The $k_{z,i}$ and $k_{z,f}$ quantities are the z components (normal to the interface) of the incident and outgoing wave vectors, respectively, and $q_{z,1} = k_{z,f} - k_{z,i}$, $q_{z,2} = k_{z,f} + k_{z,i}$, $q_{z,3} = -k_{z,f} - k_{z,i}$, $q_{z,4} = -k_{z,f} + k_{z,i}$ are the z components of the wave vector transfer for the first, second, third, and fourth scattering channels of DWBA (Figure 3), respectively. Functions $F_1(q_x, q_y, q_{z,1}, R) = F(q_x, q_y, q_{z,1}, R)$, $F_2(q_x, q_y, q_{z,2}, R) = r(\alpha_i) F(q_x, q_y, q_{z,2}, R)$, $F_3(q_x, q_y, q_{z,3}, R) = r(\alpha_f) F(q_x, q_y, q_{z,3}, R)$, $F_4(q_x, q_y, q_{z,4}, R) = r(\alpha_i) r(\alpha_f) F(q_x, q_y, q_{z,4}, R)$ are particular form factors of the DWBA model where $F(q_x, q_y, q_z, R)$ is the form factor of the spherically shaped nanoparticle with radius R at the $q = (q_x, q_y, q_z)$ point in reciprocal space, $r(\alpha_i)$ and $r(\alpha_f)$ are Fresnel reflection coefficients for the incoming and outgoing waves, respectively, and α_i and α_f are the corresponding incident and exit angles measured from the interface. The nanoparticle size dispersion was incorporated into eq 11 by a theoretical model known as the local mono-disperse approximation (LMA) of zeroth order. It assumes that the total scattering cross section is given as an incoherent sum of the intensity contributions originating from the domains consisting of nanoparticles of the same size and weighted according to their size distribution.²⁰

In the next step, we will consider the nanoparticle bilayer composed of two identical hexagonal monolayers with the paracrystal disorder as described above that are mutually correlated to form a close-packed

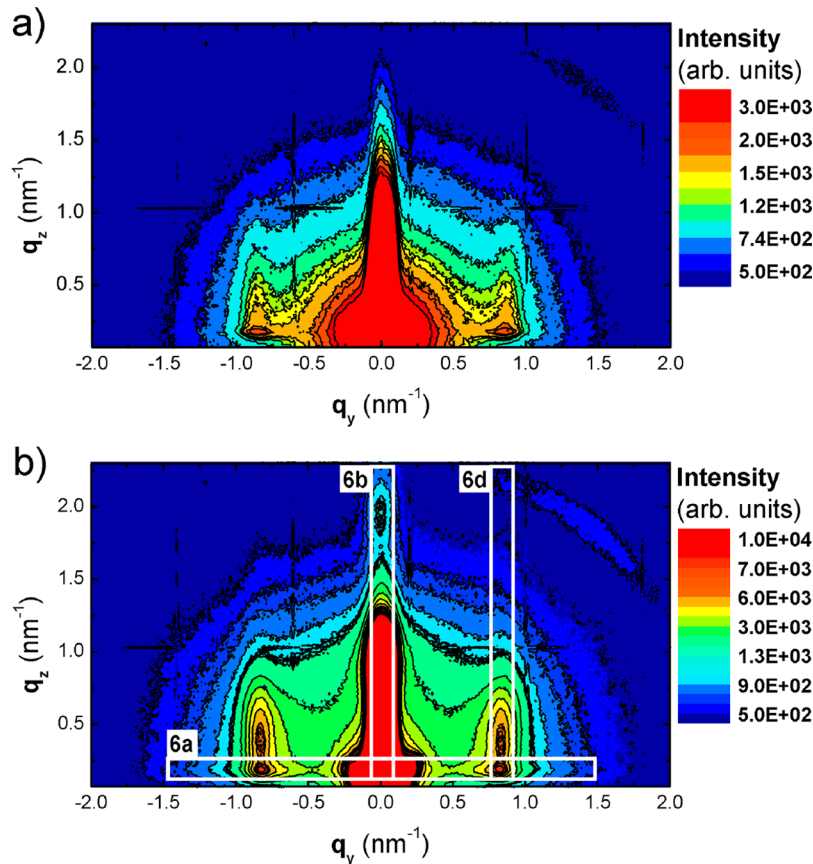


Figure 5. GISAXS pattern collected for 600 s on the silver nanoparticle Langmuir film (a) at the initial surface pressure of 9.8 mN/m before the compression started and (b) at the final surface pressure of 37.7 mN/m after the compression finished. White rectangles in b represent the regions where the intensity distributions shown in Figure 6 were evaluated.

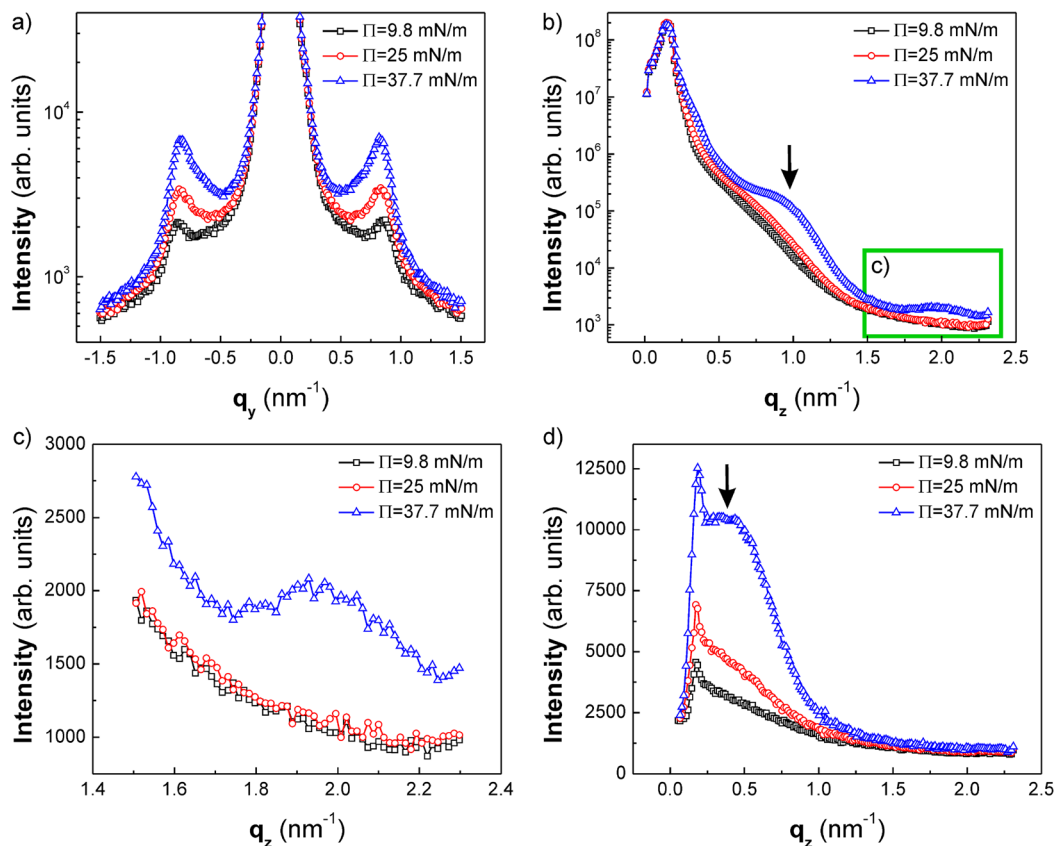


Figure 6. (a) Lateral cuts (along q_y) at the critical angle of water ($q_z = 0.18 \text{ nm}^{-1}$) and (b) vertical cuts (along q_z) at $q_y = 0.0 \text{ nm}^{-1}$ for the GISAXS patterns measured at surface pressures of 9.8, 25, and 37.7 mN/m. (c) Enlarged image of the green rectangle shown in b. (d) First Bragg rod obtained by the vertical cut at $q_y = 0.85 \text{ nm}^{-1}$.

3D structure. Referring to crystallography, such a layering is called AB stacking.²¹ In the AB-stacked bilayer, the lateral shift between the two layers is given by a translation vector (Figure 4a)²¹

$$\Delta r = \left(\frac{1}{2} \langle d \rangle, \frac{\sqrt{3}}{6} \langle d \rangle \right) \quad (13)$$

Both layers consist of $N \times N$ nanoparticles. The z coordinates of the nanoparticles located in the first and second layers are $z_1 = 0$ and $z_2 = \langle c \rangle + g_z$, respectively, where $\langle c \rangle$ is the mean interlayer distance and g_z is a Gaussian random variable along the z axis with the zero mean value and variance $\langle g_z^2 \rangle = \sigma_z^2$. The ratio $\sigma_z / \langle c \rangle$ is called the vertical degree of disorder. A side view of the nanoparticle bilayer is shown in Figure 4b. Assuming the standard DWBA theory with four scattering channels (Figure 3), each nanoparticle is a source of four scattered plane waves. These plane waves experience four different interferences inside the layers and between them, namely, 1–1, 1–2, 2–1, and 2–2 using the layer numbering. Therefore, there are 16 complex intensities coming from the interference effects between the plane waves scattered by the u th and v th nanoparticles ($u, v = 1, \dots, N$). Following the previously introduced notation, we can write equations of the scattering intensities for the four particular interference events as

$$\begin{aligned} Z_{11,st}(q_x, q_y, q_{z,s}, q_{z,t}) \\ = \sum_{s=1}^4 \sum_{t=1}^4 \langle F_s(q_x, q_y, q_{z,s}, R) F_t^*(q_x, q_y, q_{z,t}, R) \rangle_R \\ \times S_1(q_x, q_y) S_2(q_x, q_y) \end{aligned} \quad (14)$$

$$\begin{aligned} Z_{12,st}(q_x, q_y, q_{z,s}, q_{z,t}) \\ = \sum_{s=1}^4 \sum_{t=1}^4 \langle F_s(q_x, q_y, q_{z,s}, R) F_t^*(q_x, q_y, q_{z,t}, R) \rangle_R \\ \times S_1(q_x, q_y) S_2(q_x, q_y) \exp \left(-i \left(\frac{1}{2} q_x + \frac{\sqrt{3}}{6} q_y \right) \langle d \rangle \right) \\ \times \exp(-i(q_{z,t} + q_{0,t})(\langle c \rangle + g_{z,1})) \end{aligned} \quad (15)$$

$$\begin{aligned} Z_{21,st}(q_x, q_y, q_{z,s}, q_{z,t}) \\ = \sum_{s=1}^4 \sum_{t=1}^4 \langle F_s(q_x, q_y, q_{z,s}, R) F_t^*(q_x, q_y, q_{z,t}, R) \rangle_R \\ \times S_1(q_x, q_y) S_2(q_x, q_y) \exp \left(i \left(\frac{1}{2} q_x + \frac{\sqrt{3}}{6} q_y \right) \langle d \rangle \right) \\ \times \exp(i(q_{z,s} + q_{0,s})(\langle c \rangle + g_{z,2})) \end{aligned} \quad (16)$$

$$\begin{aligned} Z_{22,st}(q_x, q_y, q_{z,s}, q_{z,t}) \\ = \sum_{s=1}^4 \sum_{t=1}^4 \langle F_s(q_x, q_y, q_{z,s}, R) F_t^*(q_x, q_y, q_{z,t}, R) \rangle_R \\ \times S_1(q_x, q_y) S_2(q_x, q_y) \\ \times \exp(i((q_{z,s} + q_{0,s}) - (q_{z,t} + q_{0,t})) \langle c \rangle) \\ \times \exp(i((q_{z,s} + q_{0,s})g_{z,2} - (q_{z,t} + q_{0,t})g_{z,1})) \end{aligned} \quad (17)$$

where indices s and t represent particular channels of DWBA ($s, t = 1, \dots, 4$). $S_1(q_x, q_y)$ and $S_2(q_x, q_y)$ are given by eqs 5 and 6. The bilayer model also includes additional optical phase shifts corresponding to the geometric distance between the nanoparticle in the second layer and the air/water interface. These supplementary optical paths for the four scattering DWBA channels are determined by wave vector transfers $q_{0,1} = 0$, $q_{0,2} = 2k_0 \sin(\alpha_i)$, $q_{0,3} = 2k_0 \sin(\alpha_t)$, and $q_{0,4} = 2k_0 (\sin(\alpha_i) + \sin(\alpha_t))$, where $k_0 = 2\pi/\lambda$ is the wavenumber of the monochromatic X-ray beam and λ is the X-ray wavelength (Figure 3). The averaging of eqs 14–17 thus results in

$$\begin{aligned} \langle Z_{11,st}(q_x, q_y, q_{z,s}, q_{z,t}) \rangle \\ = \sum_{s=1}^4 \sum_{t=1}^4 \langle F_s(q_x, q_y, q_{z,s}, R) F_t^*(q_x, q_y, q_{z,t}, R) \rangle_R \\ \times \langle S_1(q_x, q_y) \rangle \langle S_2(q_x, q_y) \rangle \end{aligned} \quad (18)$$

$$\begin{aligned} \langle Z_{12,st}(q_x, q_y, q_{z,s}, q_{z,t}) \rangle \\ = \sum_{s=1}^4 \sum_{t=1}^4 \langle F_s(q_x, q_y, q_{z,s}, R) F_t^*(q_x, q_y, q_{z,t}, R) \rangle_R \\ \times \langle S_1(q_x, q_y) \rangle \langle S_2(q_x, q_y) \rangle \exp\left(-i\left(\frac{1}{2}q_x + \frac{\sqrt{3}}{6}q_y\right)\langle d \rangle\right) \\ \times \exp(-i(q_{z,t} + q_{0,t})\langle c \rangle) \exp\left(-\frac{1}{2}(q_{z,t} + q_{0,t})^2 \sigma_z^2\right) \end{aligned} \quad (19)$$

$$\begin{aligned} \langle Z_{21,st}(q_x, q_y, q_{z,s}, q_{z,t}) \rangle \\ = \sum_{s=1}^4 \sum_{t=1}^4 \langle F_s(q_x, q_y, q_{z,s}, R) F_t^*(q_x, q_y, q_{z,t}, R) \rangle_R \\ \times \langle S_1(q_x, q_y) \rangle \langle S_2(q_x, q_y) \rangle \exp\left(i\left(\frac{1}{2}q_x + \frac{\sqrt{3}}{6}q_y\right)\langle d \rangle\right) \\ \times \exp(i(q_{z,s} + q_{0,s})\langle c \rangle) \exp\left(-\frac{1}{2}(q_{z,s} + q_{0,s})^2 \sigma_z^2\right) \end{aligned} \quad (20)$$

$$\begin{aligned} \langle Z_{22,st}(q_x, q_y, q_{z,s}, q_{z,t}) \rangle \\ = \sum_{s=1}^4 \sum_{t=1}^4 \langle F_s(q_x, q_y, q_{z,s}, R) F_t^*(q_x, q_y, q_{z,t}, R) \rangle_R \\ \times \langle S_1(q_x, q_y) \rangle \langle S_2(q_x, q_y) \rangle \\ \times \exp(i((q_{z,s} + q_{0,s}) - (q_{z,t} + q_{0,t}))\langle c \rangle) \\ \times \exp\left(-\frac{1}{2}((q_{z,s} + q_{0,s})^2 + (q_{z,t} + q_{0,t})^2) \sigma_z^2\right) \end{aligned} \quad (21)$$

where $\langle S_1(q_x, q_y) \rangle$ and $\langle S_2(q_x, q_y) \rangle$ are expressed by eqs 9 and 10. The averaging over the disorder parameter g_z performed with the Baker–Hausdorff theorem^{15,21} reads

$$\langle \exp(ihg_z) \rangle = \exp\left(-\frac{1}{2}h^2 \sigma_z^2\right) \quad (22)$$

where h is a constant. Therefore, the total intensity scattered by the AB-stacked nanoparticle bilayer is given by the sum

$$\begin{aligned} I(q_x, q_y, k_{z,i}, k_{z,f}) = \sum_{s=1}^4 \sum_{t=1}^4 Z_{11,st}(q_x, q_y, q_{z,s}, q_{z,t}) + Z_{12,st}(q_x, q_y, q_{z,s}, q_{z,t}) \\ + Z_{21,st}(q_x, q_y, q_{z,s}, q_{z,t}) + Z_{22,st}(q_x, q_y, q_{z,s}, q_{z,t}) \end{aligned} \quad (23)$$

The model introduced above relies on the paracrystal monolayer and bilayer domains with in-plane hexagonal symmetry and paracrystal disorder σ . The GISAXS pattern of each such domain is inherently

asymmetric. To simulate our experimental pattern, azimuthal averaging of the X-ray intensity scattered by the nanoparticle monolayer and bilayer must be performed. To do so, the rotation of the lateral reciprocal space vector $q_{||} = (q_x, q_y)$ around the z axis is sufficient instead of the rotation of the monolayer or bilayer lattice.¹² The precession matrix used for the in-plane rotation of the reciprocal space reads

$$R(\theta)q_{||} = \begin{pmatrix} \cos(\theta) & \sin(\theta) \\ -\sin(\theta) & \cos(\theta) \end{pmatrix} \begin{pmatrix} q_x \\ q_y \end{pmatrix} \quad (24)$$

where $\theta \in \langle 0, 2\pi \rangle$ is the angle of rotation. Another way to remove the asymmetry of the calculated GISAXS pattern would be an enhancement of the paracrystal disorder σ to extremely large values, which is unrealistic because of the small size dispersion of the nanoparticles used.

RESULTS AND DISCUSSION

The GISAXS pattern collected for 600 s (1200 GISAXS frames) on the silver nanoparticle Langmuir film at the initial surface pressure of 9.8 mN/m before the compression started is shown in Figure 5a. In addition to the central intensity line along the q_z direction at $q_y = 0 \text{ nm}^{-1}$ (Bragg rod of zeroth order), there are two other ones located at $q_y = \pm 0.85 \text{ nm}^{-1}$ that indicate the presence of the lateral order induced by spontaneous nanoparticle self-assembly. The Bragg rods exhibit a peak located at $q_z = 0.18 \text{ nm}^{-1}$ that corresponds to the critical exit angle. There is only a slight modulation on the central Bragg rod indicating Langmuir film formation (see also Figure 6b). Hence, the nanoparticle coverage of the air/water interface is rather poor and the lateral order is presumably realized in the form of isolated islands. The GISAXS pattern measured for 600 s at the final surface pressure of 37.7 mN/m after the compression finished is shown in Figure 5b. The Bragg rod positions at $q_y = \pm 0.85 \text{ nm}^{-1}$ remain basically unchanged. Two new modulations around $q_z = 1.0$ and 2.0 nm^{-1} on the central Bragg rod suggest a layer stacking.

The described features of the GISAXS pattern are easily observable in Figure 6, which shows the evolution of the GISAXS pattern lateral cuts (along q_y) at the critical angle of water (Figure 6a) and the vertical cuts (along q_z) at Bragg rod positions of $q_y = 0$ and 0.85 nm^{-1} (Figure 6b,c) at surface pressures of 9.8, 25, and 37.7 mN/m. The respective GISAXS patterns were obtained by integration over 60 s (i.e., 120 GISAXS frames). This time was short enough to neglect slow changes in the GISAXS pattern at the intermediate pressure of 25 mN/m that was taken in situ during the compression. The lateral cuts (Figure 6a) exhibit a gradual intensity enhancement with increasing surface pressure as the number of nanoparticles in the X-ray-irradiated area grows during the compression. The evolution of the Bragg rod of zeroth order is shown in Figure 6b and in a more detail in Figure 6c. A slight modulation can be seen in the initial and intermediate compression stages whereas two modulations are easily observable in the final stage (the first one indicated by the black arrow). These Bragg modulations confirm a transition from poor nanoparticle coverage of the air/water interface to a closed nanoparticle Langmuir film with layer stacking. The lateral cuts indicate the presence of the lateral order from the very beginning that suggests the occurrence of ordered size-limited domains formed by the nanoparticle self-assembly. A constant position of the sharp Yoneda peak at the critical exit angle in Figure 6b indicates that the electron density contrast at the air/water interface is preserved during the compression. This fact has implications

for the GISAXS simulations. Figure 6d shows the behavior of the Bragg rod at $q_y = 0.85 \text{ nm}^{-1}$ during the compression. The most prominent feature is a huge intensity enhancement at low q_z values and the formation of a ridge in the final stage. Different from the central Bragg rod with zero lateral wave vector transfer, such a ridge formed above the Yoneda peak on any nonzero Bragg rod implies not only the presence of layering but also a nonrandom lateral shift between the positions of the nanoparticles belonging to the neighboring layers.²² In other words, the modulation observed in Figure 6d after the compression indicates a full correlation of the nanoparticle positions in both the lateral and vertical directions (i.e., the establishment of 3D-ordered nanoparticle assembly). In our particular case, the formation of a densely packed bilayer with AB-type stacking as known from crystallography is a reasonable assumption. One has to be aware, however, that the intensity distribution along the nonzero Bragg rod may also be affected by the form factor (as discussed below).

Because the X-ray beam impinged on the water surface at an angle smaller than the critical angle of water, the DWBA diffraction model developed in the previous section was fully applicable to analyze the effect of the nanoparticle order on the GISAXS pattern. To test the model, the calculations were carried out for spherically shaped nanoparticles organized into ordered domains composed of 10×10 nanoparticles in each layer. The choice of this domain size was derived from the lateral correlation length $L = 2\pi/w = 52.5 \text{ nm}$ where $w = 0.12 \text{ nm}^{-1}$ is the first lateral peak width of the final compressed nanoparticle assembly. The mean nanoparticle diameter of 5.8 nm then gives the average domain size of approximately 10×10 nanoparticles. The nanoparticle monolayer and bilayer domains were randomly azimuthally oriented via rotation in the plane of reciprocal space coordinates q_x and q_y from 0 to 359° with a step of 1° . The LMA of the zeroth order as explained in the previous section was used to include the nanoparticle size dispersion. The mean nanoparticle diameter of $5.8 \pm 0.6 \text{ nm}$ as determined by SAXS was assumed, and the mean lateral interparticle distance in the monolayer $\langle d \rangle$ and the mean interlayer distance in the bilayer $\langle c \rangle$ were derived from the positions of the nonzero Bragg rods and the position of the modulations on the central Bragg rod, respectively (Figure 6). In particular, the shortest lateral interplanar distance corresponding to $q_y = 0.85 \text{ nm}^{-1}$ reads $a = 2\pi/q_y = 7.4 \text{ nm}$, and by assuming the close-packed hexagonal lateral order, we arrive at the mean lateral interparticle distance of $\langle d \rangle = 2a/3^{1/2} \approx 8.5 \text{ nm}$. The mean vertical interlayer distance in the bilayer estimated from the position of the second Bragg modulation at $q_z = 2.0 \text{ nm}^{-1}$ is $\langle c \rangle = 4\pi/q_z \approx 6.0 \text{ nm}$. Figure 7 shows the effect of the lateral paracrystal disorder on the calculated GISAXS pattern of the nanoparticle close-packed monolayer. The pattern calculated with the degree of lateral disorder of 5% ($\sigma = 0.43 \text{ nm}$, Figure 7a) exhibits Bragg rods at $q_y = 0.85, 1.48, \text{ and } 1.7 \text{ nm}^{-1}$ that correspond to the $1:3^{1/2}:2$ sequence of the normalized coordinates characteristic of the hexagonal 2D order. In particular, the (10), (11), and (20) Bragg rods that are smeared or disappear when the degree of the lateral disorder increases to 10% ($\sigma = 0.85 \text{ nm}$, Figure 7b) can be seen. A slight modulation along the Bragg rods is due to the nanoparticle form factor. The effect of the lateral and vertical paracrystal disorder on the calculated GISAXS pattern of the close-packed nanoparticle bilayer with the AB stacking is shown in Figure 8. The pattern with identical values of the lateral and vertical degrees of disorder of 5% ($\sigma = 0.43 \text{ nm}$, $\sigma_z = 0.3 \text{ nm}$; Figure 8a) exhibits Bragg rods at the same q_y positions

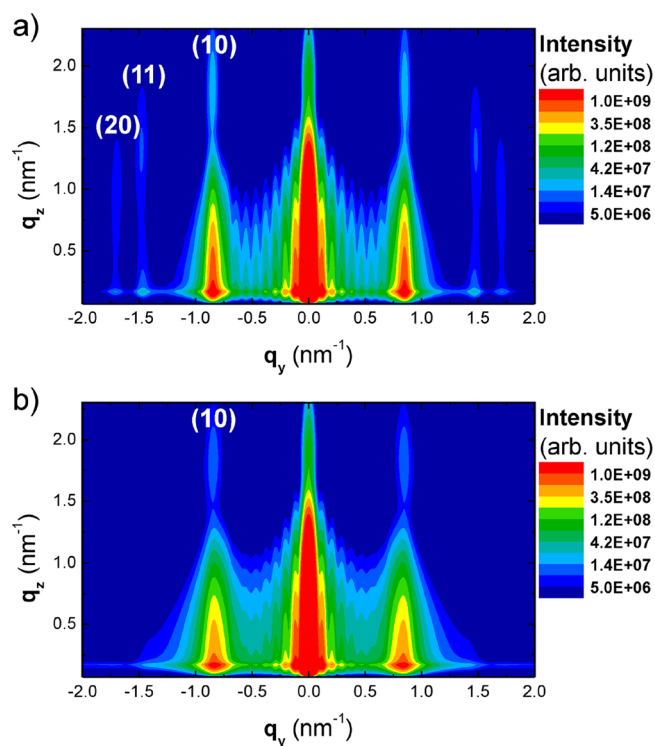


Figure 7. Theoretical GISAXS patterns calculated for randomly azimuthally oriented nanoparticle monolayer domains of limited size with lateral degrees of disorder of (a) 5 and (b) 10%.

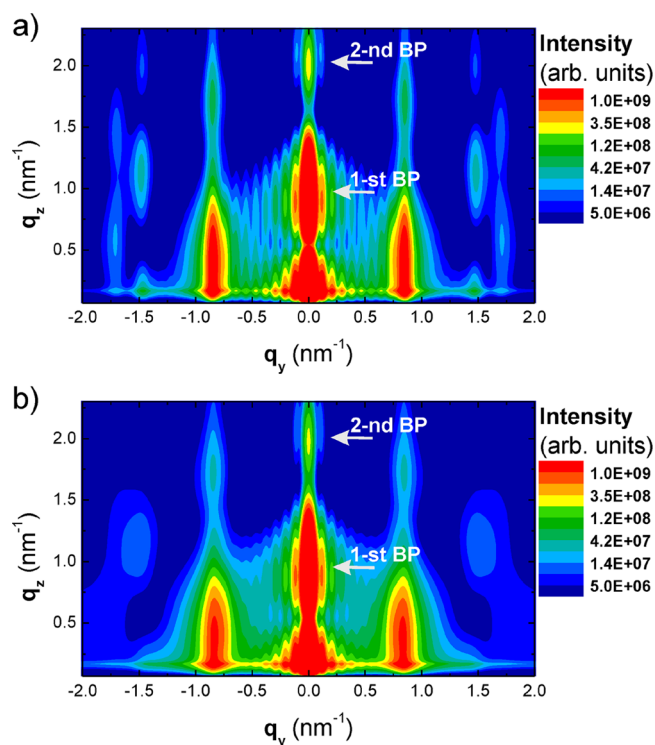


Figure 8. Theoretical GISAXS patterns calculated for randomly azimuthally oriented nanoparticle bilayer domains of limited size with lateral degrees of disorder of (a) 5 and (b) 10%. The vertical degrees of disorder were set to (a) 5 and (b) 10%.

as those in Figure 7a; however, some modulations appear along q_z because of the vertical correlations. These are rather broad

and are also slightly affected by the nanoparticle form factor. Increases in the lateral and vertical degrees of paracrystal disorder to 10% ($\sigma = 0.85$ nm, $\sigma_z = 0.6$ nm, Figure 8b) bring about the smearing or disappearance of the Bragg rods, as also observed in Figure 7b. The absence of the (11) and (20) Bragg rods in the experimental GISAXS patterns (Figure 5) and their comparison with the theoretical ones suggest a lateral degree of paracrystal disorder of around 10%. This number agrees well

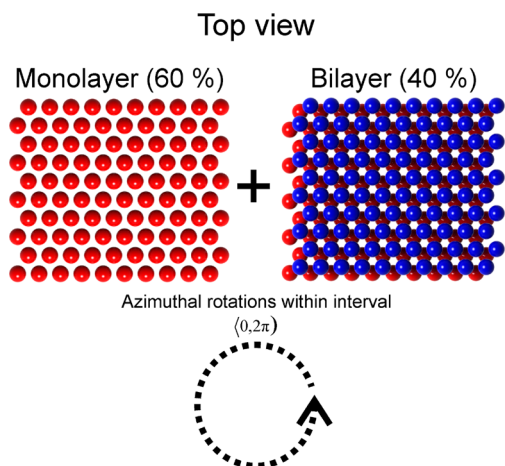


Figure 9. Model of the nanoparticle Langmuir film used for the GISAXS simulation at the final surface pressure of 37.7 mN/m. The mixture consists of randomly azimuthally oriented nanoparticle monolayer (60% coverage) and bilayer (40% coverage) domains.

with the nanoparticle size dispersion as determined from SAXS. Indeed, the size dispersion controls the regularity of the close-packed nanoparticle structure.

The diffraction model was applied to simulate the GISAXS pattern at a final surface pressure of 37.7 mN/m (Figure 5b). A comparison of the experiment (see also Figures 6b,c) with the GISAXS pattern calculated for the bilayer (Figure 8) shows that even the vertical disorder of 10% does not sufficiently damp the oscillations on the zeroth-order Bragg rod to simulate the experiment. There are two principal ways of increasing the damping: either further increasing the vertical disorder in a compact bilayer or in assuming partial bilayer coverage of the air/water interface with the monolayer in the rest of the bilayer. The first way leads to extremely large unrealistic values of the vertical disorder amounting to 50%. Therefore, the final GISAXS pattern was treated as an incoherent sum of appropriately weighted total scattering cross sections of the azimuthally averaged monolayer and bilayer

$$I(q_x, q_y, k_{z,i}, k_{z,f}) = w_{\text{mono}} I_{\text{mono}}(q_x, q_y, k_{z,i}, k_{z,f}) + w_{\text{bi}} I_{\text{bi}}(q_x, q_y, k_{z,i}, k_{z,f}) \quad (25)$$

where w_{mono} and w_{bi} are the statistical weights of the total scattering cross sections of the randomly oriented monolayer and bilayer domains, respectively, that fulfill the normalization condition $w_{\text{mono}} + w_{\text{bi}} = 1$. As in the GISAXS region the curvature of the Ewald sphere can be almost neglected (i.e., $q_x \approx 0.0$ nm⁻¹) and $q_y = 0$ nm⁻¹ for the zeroth-order Bragg rod, the fitting of this rod can be done independently of the lateral

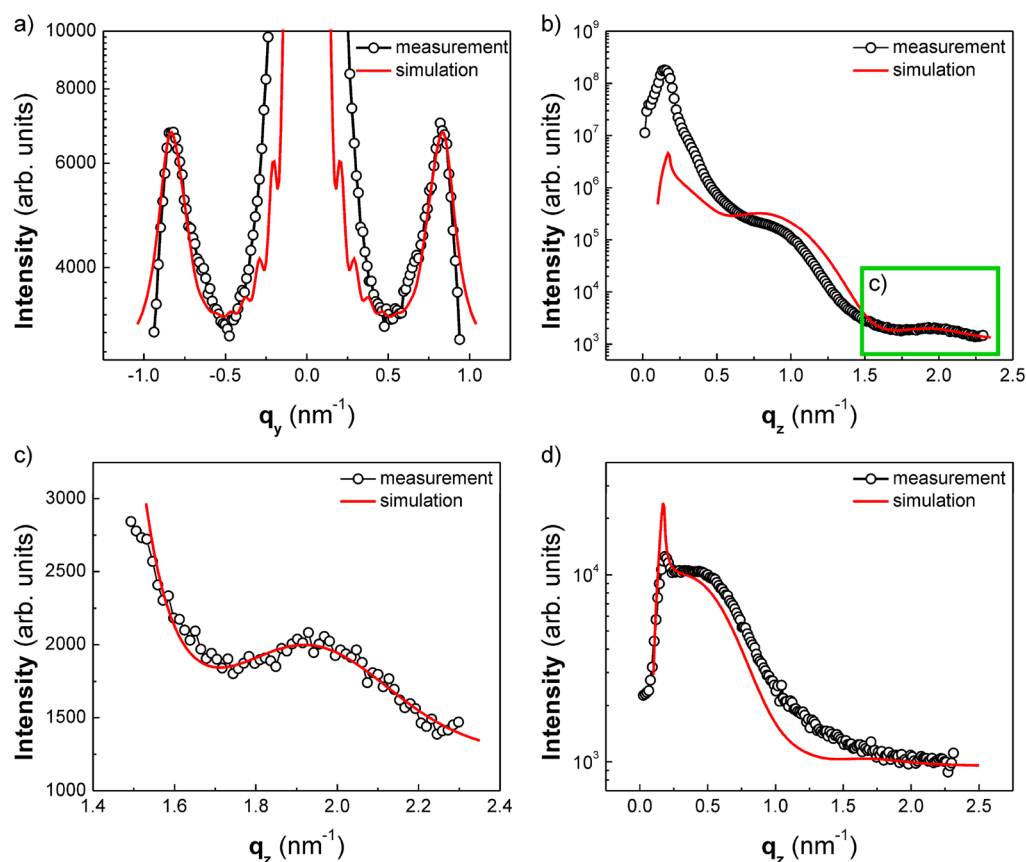


Figure 10. Lateral and vertical cuts of the GISAXS pattern measured at a final surface pressure of 37.7 mN/m (open circles) and their simulations (lines). Parts a–d are analogous to those shown in Figure 6.

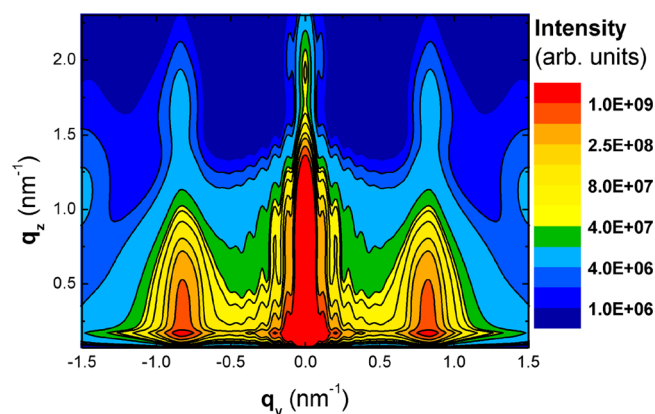


Figure 11. Theoretical simulation of the GISAXS pattern measured at a final surface pressure of 37.7 mN/m. Coverages of 60 and 40% by randomly azimuthally oriented monolayer and bilayer domains, respectively, were considered (Figure 9). The domains consisted of 10×10 nanoparticles with hexagonal paracrystal disorder. The lateral interparticle distance was set to 8.5 ± 1.0 nm, and the position of the second layer in the bilayer domain was set to 5.8 ± 0.5 nm.

paracrystal parameters. When we set the mean vertical interlayer distance to $\langle c \rangle = 6.0$ nm as calculated above and the vertical standard deviation to $\sigma_z = 0.0$ nm, the values $w_{\text{mono}} = 0.6$ and $w_{\text{bi}} = 0.4$ provided the best fit of the first modulation at $q_z \approx 1.0 \text{ nm}^{-1}$ for the zeroth-order Bragg rod visible in Figure 6b. In other words, 60% of the air/water interface irradiated by the X-ray beam is covered by the monolayer and 40% is covered by the bilayer domains (Figure 9). In the next step, the fitting of the second modulation of the zeroth-order Bragg rod enlarged in Figure 6c with weighting factors w_{mono} and w_{bi} as determined above was applied to refine the values of the mean vertical interlayer distance and the vertical standard deviation to $\langle c \rangle = 5.8$ nm and $\sigma_z = 0.5$ nm, respectively. Hence, the vertical degree of disorder of the second layer is 8.6%. The final fit is shown in Figure 10b,c. Taking the optimized parameters of the zeroth-order Bragg rod fitting, we further fitted the horizontal cut of the GISAXS pattern obtained at the critical angle shown in Figure 6a to get the values of the mean lateral interparticle distance and the lateral standard deviation of the hexagonal paracrystal $\langle d \rangle = 8.5$ nm and $\sigma = 1$ nm, respectively. This result agrees with the distance calculated directly from the experimental GISAXS pattern (see above), and the lateral degree of disorder amounts to 11.8%. The fit is shown in Figure 10a. Having all the lateral and vertical parameters available, we were able to calculate the (10) Bragg-rod-like parameters depicted in Figure 6d and arrived at very good agreement with the experiment (Figure 10d), confirming the validity of the derived parameters. In particular, a ridge above the critical angle suggesting the presence of the AB stacking is well reproduced. Finally, the whole GISAXS pattern was calculated (Figure 11) and agrees well with the experimental one at the final surface pressure (Figure 5b).

CONCLUSIONS

An original diffraction model for the analysis of the GISAXS patterns of the nanoparticle Langmuir films based on the concept of a 2D hexagonal paracrystal was developed. The model employs the DWBA formalism that is necessary at the angle of incidence close to the critical value as required for GISAXS probing of the Langmuir films. The model comprises the cases of close-packed nanoparticle monolayers and bilayers, thus

enabling us to analyze different compression stages starting from the submonolayer to the monolayer collapse via bilayer formation. This ability was demonstrated on a silver nanoparticle Langmuir film compressed at the air/water interface. The mean lateral interparticle distance, degree of the lateral paracrystal disorder, interlayer distance with standard deviation (vertical disorder) in the newly formed bilayer, layer stacking type, and ratio between the monolayer and bilayer coverage in the final film could be quantified. The model is applicable to any nanoparticle Langmuir film formed at the air/liquid interface to extract structural parameters at the nanoscale and relate them to macroscopic behavior probed by other techniques such as the surface pressure and surface potential measurements, Brewster angle and fluorescence microscopy, surface plasmon resonance, imaging, and spectroscopic ellipsometry. The particular results obtained have direct implications for the preparation of silver plasmonic templates with hot spots for surface-enhanced Raman scattering.

AUTHOR INFORMATION

Corresponding Author

*E-mail: karol.vegso@savba.sk

Notes

The authors declare no competing financial interest.

ACKNOWLEDGMENTS

The work was done during the implementation of the project Applied Research of Advanced Photovoltaic Cells, ITMS code 26240220047 (50%), supported by the Research and Development Operational Programme funded by the ERDF. The support of grant agency VEGA Bratislava, project no. 2/0041/11, and project Centre of Excellence SAS for Functionalized Multiphase Materials FUN-MAT is also acknowledged.

REFERENCES

- (1) Murray, C. B.; Kagan, C. R.; Bawendi, M. G. Synthesis and Characterization of Monodisperse Nanocrystals and Close-Packed Nanocrystal Assemblies. *Annu. Rev. Mater. Sci.* **2000**, *30*, 545–610.
- (2) Galisteo-López, J. F.; Ibisate, M.; Sapienza, R.; Froufe-Pérez, L. S.; Blanco, Á.; López, C. Self-Assembled Photonic Structures. *Adv. Mater.* **2011**, *23*, 30–69.
- (3) Colson, P.; Cloots, R.; Henrist, C. Experimental Design Applied to Spin Coating of 2D Colloidal Crystal Masks: A Relevant Method? *Langmuir* **2011**, *27*, 12800–12806.
- (4) Holmberg, K. *Handbook of Applied Surface and Colloid Chemistry*; Wiley: New York, 2002.
- (5) Martin, M. N.; Basham, J. I.; Chando, P.; Eah, S.-K. Charged Gold Nanoparticles in Non-Polar Solvents: 10-min Synthesis and 2D Self-Assembly. *Langmuir* **2010**, *26*, 7410–7417.
- (6) Kim, B.; Carignano, M. A.; Tripp, S. L.; Wei, A. Cluster Size Analysis of Two-Dimensional Order in Colloidal Gold Nanoparticle Arrays. *Langmuir* **2004**, *20*, 9360–9365.
- (7) Fukuto, M.; Heilmann, R. K.; Pershan, P. S.; Badia, A.; Lennox, R. B. Monolayer/Bilayer Transition in Langmuir Films of Derivatized Gold Nanoparticles at the Gas/Water Interface: An X-ray Scattering Study. *J. Chem. Phys.* **2004**, *120*, 3446–3459.
- (8) Schultz, D. G.; Lin, X.-M.; Li, D.; Gebhardt, J.; Meron, M.; Viccaro, J.; Lin, B. Structure, Wrinkling, and Reversibility of Langmuir Monolayers of Gold Nanoparticles. *J. Phys. Chem. B* **2006**, *110*, 24522–24529.
- (9) Kim, K.; Leahy, B. D.; Dai, Y.; Shpyrko, O.; Soltau, J. S.; Pelton, M.; Meron, M.; Lin, B. Governing Factors in Stress Response of Nanoparticle Films on Water Surface. *J. Appl. Phys.* **2011**, *110*, 102218–.

- (10) Pohjalainen, E.; Pohjakallio, M.; Johans, C.; Kontturi, K. s.; Timonen, J. V. I.; Ikkala, O.; Ras, R. H. A.; Viitala, T.; Heino, M. T.; Seppälä, E. T. Cobalt Nanoparticle Langmuir–Schaefer Films on Ethylene Glycol Subphase. *Langmuir* **2010**, *26*, 13937–13943.
- (11) Tolan, M. *X-ray Scattering from Soft-Matter Thin Films Materials Science and Basic Research*; Springer: Berlin, 1999.
- (12) Sun, Y.; Frenkel, A. I.; Isseroff, R.; Shonbrun, C.; Forman, M.; Shin, K.; Koga, T.; White, H.; Zhang, L.; Zhu, Y.; Rafailovich, M. H.; Sokolov, J. C. Characterization of Palladium Nanoparticles by Using X-ray Reflectivity, EXAFS, and Electron Microscopy. *Langmuir* **2005**, *22*, 807–816.
- (13) Vegso, K.; Siffalovic, P.; Weis, M.; Jergel, M.; Benkovicova, M.; Majkova, E.; Chitu, L.; Halahovets, Y.; Luby, S.; Capek, I.; Satka, A. In situ GISAXS Monitoring of Langmuir Nanoparticle Multilayer Degradation Processes Induced by UV Photolysis. *Phys. Status Solidi A* **2011**, *208*, 2629–2634.
- (14) Renaud, G.; Lazzari, R.; Leroy, F. Probing Surface and Interface Morphology with Grazing Incidence Small Angle X-ray Scattering. *Surf. Sci. Rep.* **2009**, *64*, 255–380.
- (15) Millane, R. P.; Eads, J. L. Diffraction by One-Dimensional Paracrystals and Perturbed Lattices. *Acta Crystallogr., A* **2000**, *56*, 497–506.
- (16) Mu, X. Q. X-ray Diffraction by a One-Dimensional Paracrystal of Limited Size. *Acta Crystallogr., A* **1998**, *54*, 606–616.
- (17) Eads, J. L.; Millane, R. P. Diffraction by the Ideal Paracrystal. *Acta Crystallogr., A* **2001**, *57*, 507–517.
- (18) Sinha, S. K.; Sirota, E. B.; Garoff, S.; Stanley, H. B. X-ray and Neutron-Scattering from Rough Surfaces. *Phys. Rev. B* **1988**, *38*, 2297–2311.
- (19) Siffalovic, P.; Vegso, K.; Jergel, M.; Majkova, E.; Keckes, J.; Maier, G. A.; Cornejo, M.; Ziberi, B.; Frost, F.; Hasse, B.; Wiesmann, J. Measurement of Nanopatterned Surfaces by Real and Reciprocal Space Techniques. *Meas. Sci. Rev.* **2010**, *10*, 153–156.
- (20) Lazzari, R. IsGISAXS: a Program for Grazing-Incidence Small-Angle X-ray Scattering Analysis of Supported Islands. *J. Appl. Crystallogr.* **2002**, *35*, 406–421.
- (21) Hammond, C. *The Basics of Crystallography and Diffraction*, 3rd ed.; Oxford University Press: Oxford, U.K., 2009.
- (22) Vegso, K.; Siffalovic, P.; Benkovicova, M.; Jergel, M.; Luby, S.; Majkova, E.; Capek, I.; Kocsis, T.; Perlich, J.; Roth, S. V. GISAXS Analysis of 3D Nanoparticle Assemblies—Effect of Vertical Nanoparticle Ordering. *Nanotechnology* **2012**, *23*, 045704.